



UNIVERSITY OF LEEDS

This is a repository copy of *Modeling the heart*.

White Rose Research Online URL for this paper:
<http://eprints.whiterose.ac.uk/145141/>

Version: Accepted Version

Book Section:

Colman, MA orcid.org/0000-0003-2817-8508 and Holden, AV (2019) *Modeling the heart*.
In: *Encyclopedia of Biophysics*. Springer .

https://doi.org/10.1007/978-3-642-35943-9_379-1

© European Biophysical Societies' Association (EBSA) 2019. This is a post-peer-review, pre-copyedit version of a chapter published in *Encyclopedia of Biophysics Living Edition*. The final authenticated version is available online at: https://doi.org/10.1007/978-3-642-35943-9_379-1

Reuse

Items deposited in White Rose Research Online are protected by copyright, with all rights reserved unless indicated otherwise. They may be downloaded and/or printed for private study, or other acts as permitted by national copyright laws. The publisher or other rights holders may allow further reproduction and re-use of the full text version. This is indicated by the licence information on the White Rose Research Online record for the item.

Takedown

If you consider content in White Rose Research Online to be in breach of UK law, please notify us by emailing eprints@whiterose.ac.uk including the URL of the record and the reason for the withdrawal request.



eprints@whiterose.ac.uk
<https://eprints.whiterose.ac.uk/>

© European Biophysical Societies' Association (EBSA) 2013

Gordon C. K. Roberts

Encyclopedia of Biophysics

10.1007/978-3-642-16712-6_379

Modeling the Heart

Michael A. Colman¹ and Arun V. Holden¹

(1)School of Biomedical Sciences, University of Leeds, Leeds, LS2 9JT, UK

Arun V. Holden

Email: A.V.Holden@leeds.ac.uk

Without Abstract

Synonyms

[Action potentials](#); [Cardiac physiome](#)

Definition

Quantitative prediction over multiple space and time scales using computer models of the electrical activity in the mammalian heart, based on membrane and intracellular ion transport and binding dynamics, digital histology, and three-dimensional cardiac anatomy and architecture.

Introduction

The normal rhythmic beating of the heart is triggered by repetitive waves of depolarization (propagating action potentials) that spread from the pacemaking sinoatrial node, through the atria and conducting system (atrioventricular node, Bundle of His and Purkinje fibers) to the ventricular tissue, producing the synchronized atrial, followed by ventricular, contractions that form one cycle of the heart beat. Calcium entry during depolarization triggers calcium induced calcium release from the intracellular sarcoplasmic reticulum, and the rise in intracellular calcium triggers contraction. The essential features are autorhythmicity - the isolated heart continues to beat, and the synchronization produced by fast (up to 1 m/s) propagation. The repetitive pumping drives the circulation, and loss of synchronous cardiac contractions, as in cardiac arrhythmias, can rapidly lead to death. Computational modeling of the interactions among a few dozen membrane proteins – ligand- or voltage-gated ion channels that are characterized by their ionic selectivities, kinetics and pharmacology, ion pumps and exchangers, and connexins forming intercellular gap junctions; and intracellular ion binding, sequestration and release, within the tissue architecture and geometry of the heart can account for these processes, and predict the cell, tissue and whole heart level effects of differences in specific channel kinetics or densities that result from gender, remodeling, mutations, drugs, or disease (Panfilov and Holden [1997](#); Roberts et al 2012).

Cardiac Membrane and Cell Excitation

A single cardiac myocyte, isolated by enzymic digestion, or a small spheroid of cells grown in gyratory cell culture, or a small ball of myocardial tissue are all too small for membrane potential V to change with distance, and so are effectively isopotential, with $dV/dt = -I_{ion}(V)/C$, where $I_{ion}(V)$ is a function representing how the total ionic current depends on voltage, and C the capacitance, of either a cell or a unit area of membrane. This can be obtained by the analysis of macroscopic currents obtained from whole cell microelectrode recording techniques. For autorhythmicity or excitability, $f(V)$ is nonlinear, with the characteristics of a cubic. If the equilibrium solution at which $dV/dt = 0$ is stable (all the eigenvalues have negative real parts) the system is excitable, and the threshold is at the negative slope intercept of the zero current axis. If the equilibrium solution is unstable and a complex conjugate pair of eigenvalues have positive real parts then the solution is oscillatory and the system is autorhythmic (pacemaking). Whether a myocyte is pacemaking or excitable depends on the stability of its equilibrium solution. The stability depends on the parameters that control current magnitudes (maximal channel conductances/channel densities), and parameters that determine the channel gating kinetics.

The first model of a cardiac action potential in terms of ionic mechanisms (Noble [1962](#)) was a modification the Hodgkin-Huxley equations to reproduce the prolonged Purkinje fiber action potential, and its automaticity. Cardiac action potential models are reconstructed from a number of membrane ionic currents, through channels, pumps, and exchangers. A current is characterized by its ion-selectivity, pharmacology, kinetics, and voltage- or ligand-dependence, recorded under voltage clamp, in macroscopic in vitro experiments on small isopotential preparations, or in patch-clamp experiments on channels expressed in amphibian eggs or mammalian cell lines. The cardiac action potential is generated by inward (Na^+ and Ca^{++}), outward (K^+), pacemaking, background and stretch-activated currents through ion channels (Priest and McDermott 2015). Single channel currents are of the order of a pA, i.e., $\sim 10^6$ ions/s, and current flow through an open channel is by electrodiffusion, by binding to multiple binding sites within the channel.

The instantaneous current voltage relation can be linear, and given by the product of a conductance G and a driving force, as background currents, for the Na^+ background current:

$$I_{Na} = G_{Na} (V - V_{Na})$$

and the fast Na^+ current

$$I_{Na} = g_{Na} (V - V_{Na}) = G_{Na} m^3 h j (V - V_{Na})$$

The conductance g is the product of the maximal conductance G and the fraction that is conducting; this can be controlled by separate activation and inactivation gates, (for g_{Na} m is activation, h inactivation, and j slow inactivation; $0 \leq m, h, j \leq 1$ that can be interpreted as the fraction of the gates in a state that allows ion flow, or the probability that a gate is "open").

When there is a difference in ion concentration across the membrane the Goldman-Hodgkin-Katz constant field theory equations predict a nonlinear rectifying current, (the magnitude of the current for a given driving force depends on the direction of ion flow current), and this is marked for Ca^{++} currents, where intra- and extracellular concentrations $[Ca^{++}]_i$ differ by four orders of magnitude ($[Ca^{++}]_i$ from 100 nM diastolic to 1 μ M systolic, $[Ca^{++}]_o \sim 2$ mM). For the L-type Ca current $I_{Ca,L}$

$$I_{Ca,L} = G_{Ca,L} d f_{Ca} \exp\left(\frac{4V(F^2/RT)}{RT} - 0.341 \frac{[Ca^{++}]_o}{[Ca^{++}]_i}\right) \exp\left(\frac{2VF}{RT}\right) - 1$$

where d is a voltage-dependent activation gate, f a voltage-dependent inactivation gate, and f_{Ca} a $[Ca^{++}]_i$ dependent inactivation gate; F and R are Faraday's and the gas constant, and T the absolute temperature. The 0.341 comes from the ratio of the partition coefficients for Ca^{++} .

The time dependence of ionic permeabilities and conductances with linear or nonlinear instantaneous current-voltage relationship is described by the kinetics of the activation and inactivation gating processes (m, h, j, d, f, f_{Ca} in the two examples above), that have voltage-dependent macroscopic rate coefficients of opening $\alpha(V)$ and closing $\beta(V)$ that are described by empirical expressions based on curve fitting, e.g., for the fast activation of I_{Na}

$$\alpha_m(V) = \frac{1}{1 + \exp\left(\frac{-56.86 - V}{9.03}\right)^2}$$

with analogous expressions for $\beta(V)$. An alternative and equivalent description, in place of the rate coefficients $\alpha(V)$ and $\beta(V)$, is by the time coefficient $\tau(V) = 1/(\alpha(V) + \beta(V))$, and steady-state value, e.g., $m_\infty = \alpha_m(V)/(\alpha_m(V) + \beta_m(V))$.

Single file transfer across multiple binding sites provides one mechanism for channel rectification. The strong inward rectification of K^+ channels is due to block of the channel by intracellular polyvalent cations (Hille [2001](#)), and the inward rectifier K^+ current I_{K1} is represented by:

$$I_{K1} = G_{K1} \sqrt{\frac{[K^+]_o}{5.4}} x_{K1} \exp\left(\frac{V - E_{K1}}{RT}\right)$$

where x_{K1} is a time independent rectifier factor that depends on voltage, and $\sqrt{[K^+]_o/5.4}$ describes the dependence on $[K^+]_o$.

Each current is described by terms that give its magnitude (maximal conductance G , or product of channel density and single channel conductance), gating dynamics by activation and inactivation variables, and instantaneous current voltage relation that have been obtained in extensive series of voltage clamp experiments under different conditions. The channel density (which can act as a bifurcation parameter) fluctuates, due to changes in channel regulation, and trafficking and insertion into the membrane, and so can be modeled by a stochastic variable. The analysis of patch-clamp recordings of single channel activity in terms of opening, closing, and open time probability distributions gives a microscopic interpretation of $\alpha(V)$ and $\beta(V)$ as probabilities, that are related to the transition probabilities between multiple states in Markov model within kinetic state diagrams of a single channel. Markov models allow the kinetics of drug-channel interactions to be modeled in detail. These equations for microscopic, multistate single channel currents and macroscopic membrane currents are semiempirical, and contain experimentally estimated parameters and dynamic variables, on time scales from 10 μ s to s.

There are also semiempirical expressions for pump and exchanger currents, and for intracellular ion concentration dynamics, and for $[Ca^{++}]_i$ binding and sequestration. The equations for the individual currents are constructed from currents recorded under voltage clamp, and so will reconstruct these currents. If all the membrane currents are summed as $I_{ion}(V)$ then

$$dV/dt = -I_{ion}(V)/C$$

should reconstruct $V(t)$ for the cell. However the model will require some informed manipulation, to ensure electroneutrality at rest (so at the resting membrane potential $dV/dt=0$) and electrochemical neutrality (so the individual ionic fluxes are all individually equal to zero, and there are no slow drifts in intracellular concentrations and hence potential).

Cardiac cell models are in a state of continuing development, and as a result of interactions

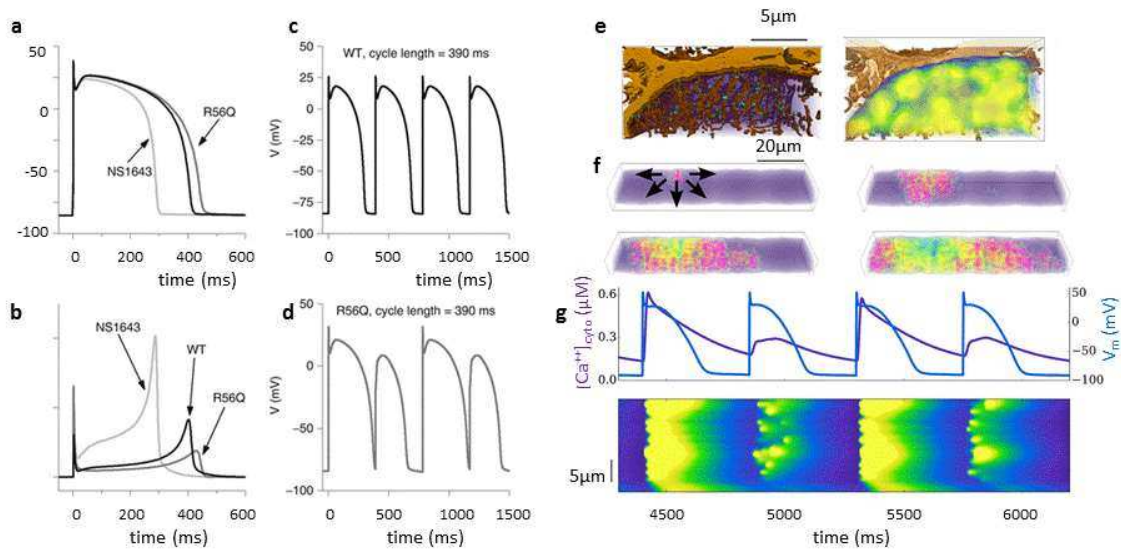
with experiment have undergone several paradigm shifts, with new mechanisms being incorporated, data being reinterpreted and some old mechanisms replaced (Noble and Rudy [2001](#)).

Families of ordinary differential equation cardiac cell models have been developed to describe the voltage and time-dependent current I_{ion} that reconstruct the action potentials $V(t)$ of different types of cardiac myocytes cells of a number of species: mouse, rat, rabbit, dog, pig, and man. Cardiac cell electrophysiology models, although simple in principle, are complicated because of the large number of dynamic variables, with kinetics over several orders of magnitude, and large number of parameters, and empirical expressions for gating variables, and so need to be specified by computer programs if they are to be used. A printed description probably contains typographical errors, or a mismatch between the equations described and the revised equations used to generate the final figures, and models are generally published with the computer code as an electronic supplement, and are available in a standard markup language such as CellML (Fink et al. [2010](#)). These stiff (have time scales from 100 μ s to 100 ms), high order (have a large number of dynamic variables) cardiac cell electrophysiology models are solved by numerical integration for time spans of seconds (during repetitive activity after more than a few seconds there are nonphysiological drifts in ionic concentration) to compute $V(t)$, with a time step of ~ 10 –100 μ s. Computing technology is now fast enough for cell $V(t)$ to be computed in close to real time on a PC, especially if efficient programming methods (adaptive time steps, use of look up tables rather than evaluation for the $\alpha(V)$ and $\beta(V)$) are used.

The qualitative nature of solutions of $V(t)$ need to be physiologically appropriate: models for isolated cells that are pacemaking (sinoatrial and atrioventricular node, Purkinje fibers) need to be autorhythmic, while models of atrial and ventricular myocytes need to have a stable equilibrium that corresponds to the resting membrane potential, and be excitable. Small changes in the value of a parameter (say a conductance) can change the stability of the equilibrium, producing a qualitative change in behavior, and allowing periodic solutions to occur. This is a bifurcation, and periodic solutions can emerge at Hopf or homoclinic bifurcation points (Ermentrout and Rinzel [2009](#)). Changes in a number of the cell model parameters can produce periodic solutions, and so pacemaking is an emergent, cell level system property, and is not due to a specific pacemaking mechanism, such as the hyperpolarization activated funny current I_f , or intracellular Ca^{++} oscillators, or multiple redundant mechanisms, where removal of one mechanism exposes another.

Figure [1](#) illustrates numerical solutions for a normal human ventricular cell model, and when the parameters have been modified to simulate a mutation that produces long-QT syndrome, and the effects of a drug whose actions on the channel kinetics are known. The action potential solutions for an excitable myocyte can be quantified by measures of its threshold (strength duration curve) and shape – resting potential, peak potential, maximum rates and rise and fall, times at which they occur, and action potential duration APD (measured as APD₉₀, time to 90% depolarization), and for an autorhythmic cell by its maximum and minimum potentials, rate and its response to brief perturbations, by a phase resetting curve (Winfree [2001](#)). These can be compared to experiments, and further model validation can be by reproducing the effects of drugs, if their actions on membrane channels have been described quantitatively. When validated, cell models can be used to predict the cell level effects of drugs whose channel level actions are known. Although antiarrhythmic drugs can be classified by what channels they act on (e.g., type 1a antiarrhythmics, such as flecainide reduce excitability by blocking I_{Na}), many antiarrhythmics act on several ion channels

(e.g., dronedarone) and can have multiple actions (e.g., the I_{Na} blocker flecainide also acts on intracellular Ca^{++} release kinetics) (Leenhardt et al 2012).



Modeling the Heart, Fig. 1

Cellular and intracellular dynamics. (a – d) Modelling effects of mutations and pharmacological agents *via* their effects on conductances and kinetics. Human mid-myocardial ventricular action potentials computed from ten Tusscher and Panfilov [2006](#) model (WT), modified for effect of a mutation in the human ether-a-go-go-related gene (hERG), which encodes the Kv11.1 potassium channel, reduces I_{Kr} , and is responsible for LQT2 syndrome (R56Q), and the effects of the hERG channel opener NS1643. (a) solitary action potentials, produced by a brief depolarizing current pulse; (b) I_{Kr} during these action potentials; (c) repetitive periodic activity in normal; (d) alternating periodic activity in mutant model, both produced by repetitive stimulation at same cycle length. (e – g) Modeling intracellular, stochastic spatio-temporal Ca^{++} dynamics. The stochastic local dynamics of Ca^{++} release units which underlie Ca^{++} sparks can lead to spontaneous Ca^{++} waves and spatial Ca^{++} transient alternans (Colman et al 2017) (e) High resolution reconstructions of the surface-sarcolemma (light-brown contour) and T-tubule (dark-brown contour) membranes from a portion of a large mammal ventricular myocyte, from electron-microscopy imaging. (Pinali et al 2013). The dyads are shown as light-blue contour dots, with a color-mapped snapshot of computed spatial Ca^{++} concentration in this portion of the cell, illustrating the non-uniformity in Ca^{++} distribution associated with normal excitation. (f) Color-mapped snapshots every 100ms of the development and propagation of an intracellular Ca^{++} wave in a model of a full cell. (g) Intracellular Ca^{++} transient alternans. The top panel shows the Ca^{++} transient (purple, left axis) and AP (blue, right axis). The lower panel is a linescan through the cell showing Ca^{++} concentration. The differences in activation patterns between the even beats accounts for the irregularity of the small amplitude Ca^{++} transients.

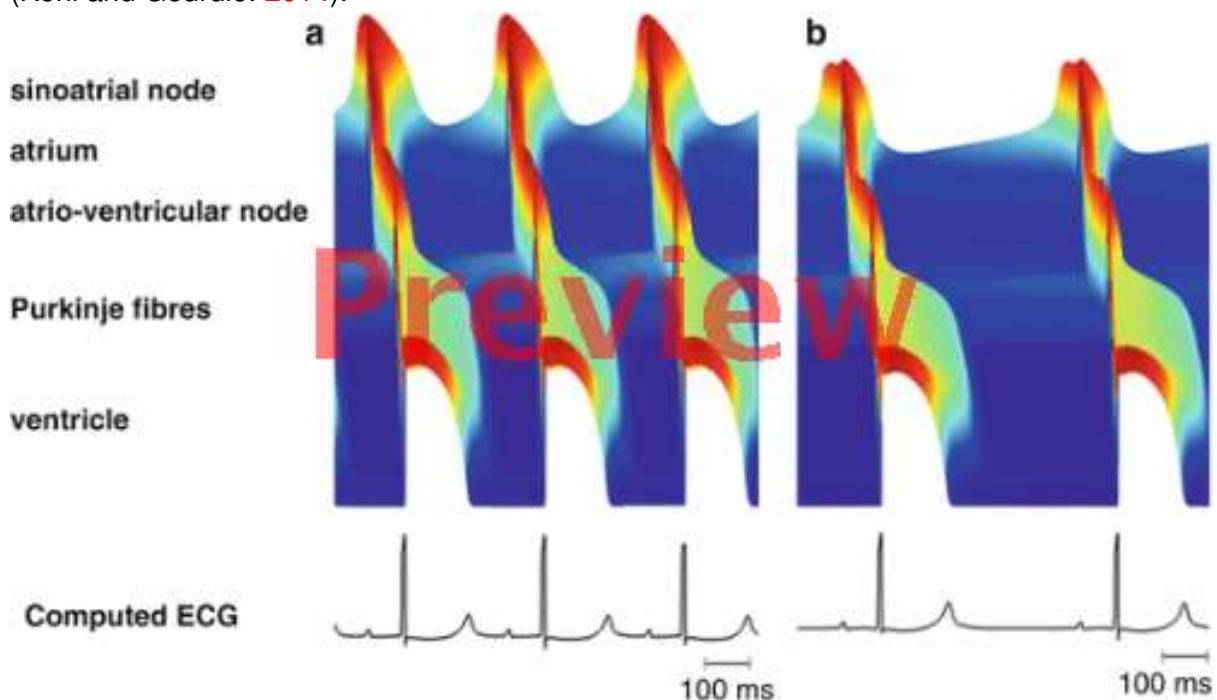
Virtual cells can also quantitatively test if the effects of inherited channelopathies (disease caused by mutations in genes coding membrane channels) account for their electrophysiological symptoms (e.g., long or short QT syndromes). Modeling pathological states, e.g., acute ischemia is complicated by actions on intracellular metabolism as well as directly on the electrophysiological processes being modeled, and chronic disease, e.g., atrial fibrillation can cause remodeling of the cell ion channels (Trayanova 2014).

If the APD restitution curve has a maximal slope >1 , then periodic action potentials at rates where the slope is >1 are unstable and a period-doubling bifurcation into alternans (a

periodic sequence of long-short APDs) is expected. Alternans in itself is benign, but prognostically is a bad sign. The maximal slope of the APD restitution curve is used as an arrhythmogenic index, and can be computed, or estimated experimentally. These cell models are all deterministic – stochasticity necessary to account for the temporal variability in cell properties can be introduced by additive noise terms, by repeated computations on a population of cell models, where some of the cell parameters are drawn from a distribution, or by stochastic models of the ionic channel mechanisms (Qu et al, 2014)

Cardiac Heterogeneity

Action potentials recorded from myocytes isolated from different points in the heart differ qualitatively (autorhythmic or excitable) and have quantitative differences in shape. Figure 2 illustrates propagating action potentials computed at different points through the cardiac pacemaking, conduction system and myocardium during normal sinus rhythm, and illustrates the wave nature of cardiac propagation. These spatial differences in action potential shape can be explained by spatial differences in the expression of different ion channel proteins. The mRNA abundance and the expressed protein density are not semiquantitative indices of the density of functionally active channels, but provide a guide for segmenting cardiac tissue and identifying different types of myocyte. Ten types of cardiac myocyte have been described, and quantitatively modeled for the rabbit heart – cells from the center and periphery of the sinoatrial node, atrial muscle fast and slow pathways of the atrioventricular node and the His bundle), Purkinje fibers and endo-, mid-, and epicardial layers of the left ventricle, where each cell type has a characteristic electrophysiology that is determined by the relative densities of the different ion channels. Cardiac tissue action potentials reflect the electrotonically smoothed local cell action potentials, and so spatial changes in tissue electrophysiology could be due to changes in the ratio for mixtures of two or more cell types (a mosaic), or to a smooth tissue gradient in the expressed channel densities. Myocardial tissue also contains inexcitable fibroblasts that may be electrically coupled to the myocytes (Kohl and Gourdie. 2014).



Modeling the Heart, Fig. 2

Space–time plot of color-coded computed membrane potential along rabbit cardiac conduction axis during (**a**) normal sinus rhythm (**b**) sinus rhythm slowed by incorporating the actions of an acetylcholine analogue. The action potential is generated in the SAN and propagates through the rest of the heart toward the ventricular epicardium as a series of repetitive waves

Cardiac Propagation

The 20–100 μm myocardial cells are coupled via low resistance gap junctions, and at the mm scale propagation appears smooth and can be modeled by a continuous, excitable medium represented by a reaction-diffusion equation:

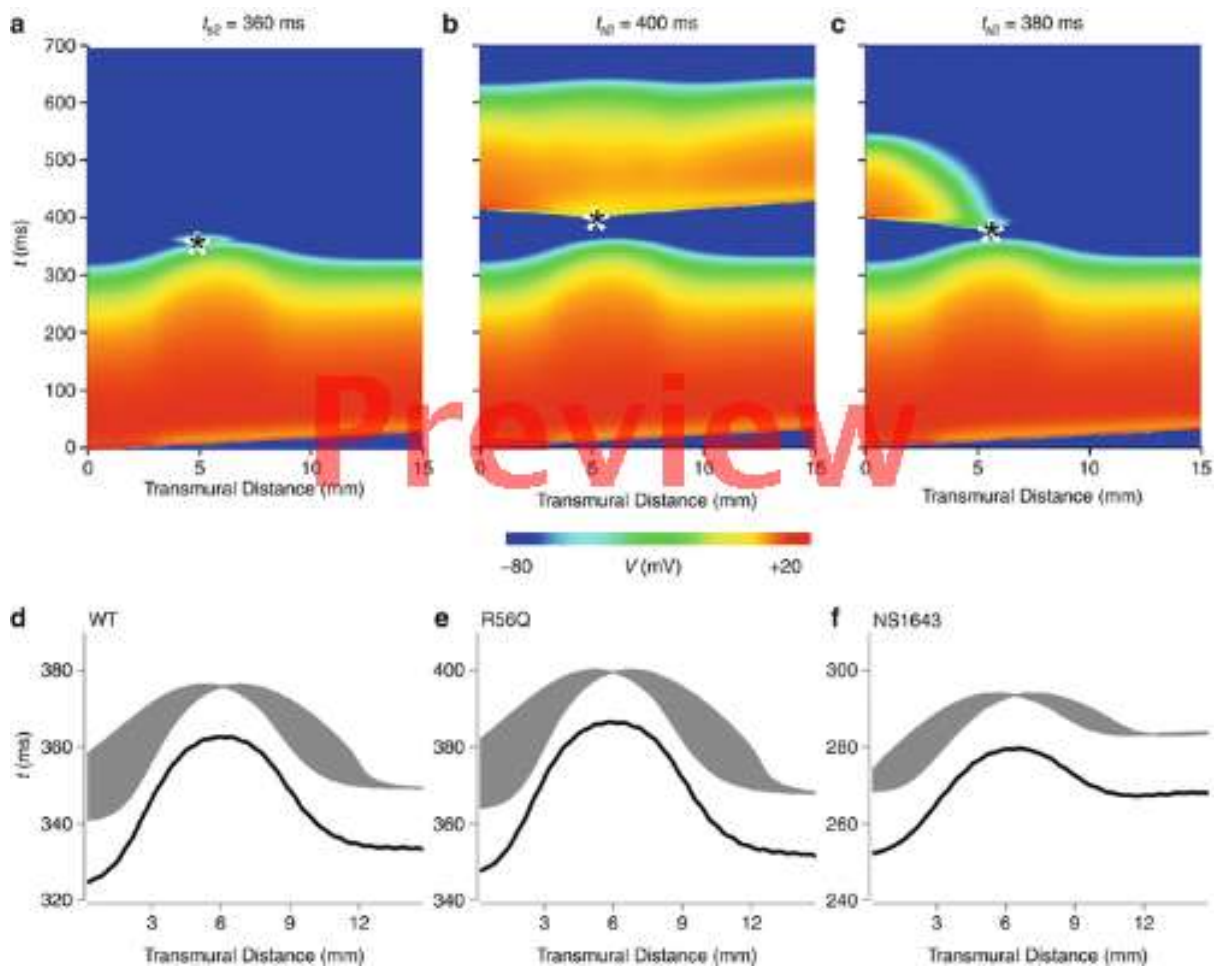
$$\frac{\partial \text{V}}{\partial \text{t}} = \nabla \cdot (D \nabla \text{V}) - I_{\text{ion}}(\text{V}).$$

(∇) is a spatial gradient operator, D is the electrical diffusion coefficient tensor ($\text{mm}^2 \text{ms}^{-1}$) that gives the spatial scale. Spatial differences in cell electrophysiology and protein expression can be mapped as spatially varying parameters in the equations for $I_{\text{ion}}(\text{V})$.

The electrical diffusion tensor D is defined within the geometry of the heart and changes with location: it is determined principally by the average orientation of myocytes at any given location. Numerical solutions requires a time step determined by the kinetics of $I_{\text{ion}}(\text{V})$ and a space step small enough to ensure numerical stability, and convergence of the traveling wave solution. These integration steps can be selected empirically, by tracking the convergence of the solution as the steps are reduced, and are typically $\sim 100 \mu\text{s}$, $\sim 100 \mu\text{m}$

The conduction velocity of a cardiac action potential depends on the membrane conductances, and intercellular coupling: via connexins, the proteins that form the gap junctions coupling myocytes, and perhaps also fibroblasts. Electrical coupling is modeled via the diffusion coefficient D : a value of D is selected to give the appropriate conduction velocity for the excitation model. Cardiac tissue possesses a complex fiber-sheet structure, and propagation is anisotropic, up to five times faster along the local myocyte orientation, and is orthotropic, faster within sheets than across sheets.

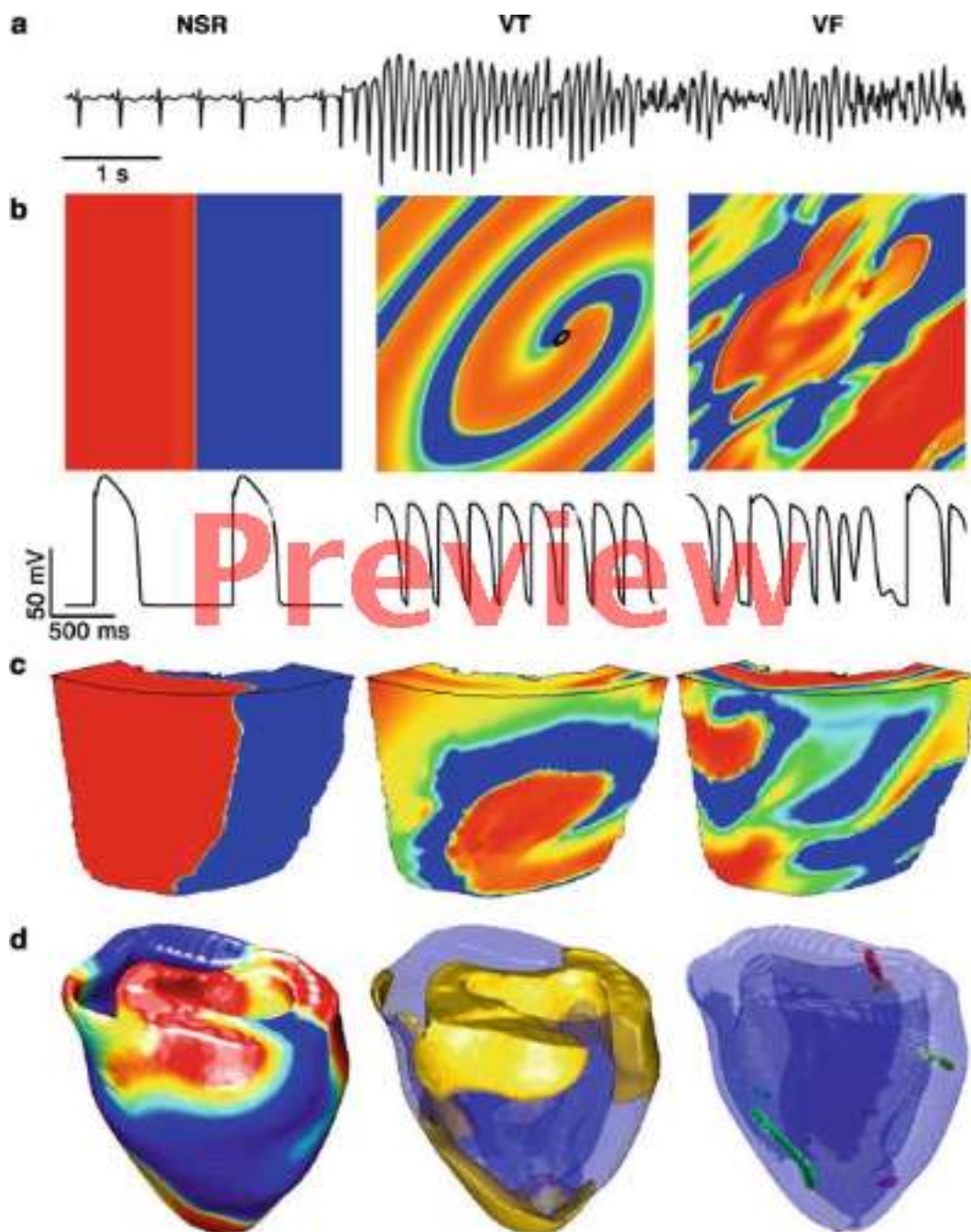
One-dimensional models can support solitary wave and wave train solutions. At higher rates, the APD is shortened, velocity is reduced, and the wavelength is shortened. Colliding traveling wave solutions annihilate each other; this destructive interference results from the refractory period of the action potential. Figure 3 illustrates the responses of a one-dimensional model to stimulation at different times in the wake of an action potential. The vulnerable window is the period after a preceding action potential during which a unidirectional wave can be initiated, i.e., there is a unidirectional conduction block. The initiation of a single solitary wave in a one-dimensional ring provides a computationally simple model for reentry; such unidirectional propagation can only be produced in a homogeneous one-dimensional medium if the symmetry is broken, say by a preceding action potential.



Modeling the Heart, Fig. 3

Computed response of human virtual ventricular wall to localized stimulation. (**a– c**) space time plots, with a S_1 stimulation at $t = 0$ on the endocardial border producing an action potential that propagates through the wall from *left to right* at a constant velocity. A second stimulus S_2 at the * produces (**a**) no response: the stimulus is in the refractory period (**b**) bidirectional propagation and (**c**) unidirectional propagation, i.e., the stimulus is in the vulnerable window. (**d– f**) the transmurial distribution of action potential duration and width of vulnerable window, for normal (WT), LQT2 mutant (R56Q), and hERG channel opener (NS1663) modified tissue

Stimulation during the vulnerable period in the wake of a plane wave in a two-dimensional medium would initiate a pair of spiral waves. The width of the vulnerable window and the transmurial dispersion in APD are indices of pro-arrhythmogenicity, i.e., the likelihood of the occurrence of a reentrant arrhythmia. Figure 4 illustrates the onset and breakdown of ventricular tachycardia into ventricular fibrillation.



Modeling the Heart, Fig. 4

Computational modeling of human ventricular fibrillation. (**a**) clinical electrocardiogram of spontaneous onset of an episode of ventricular fibrillation (VF) from normal sinus rhythm (NSR) through ventricular tachycardia (VT) (**b**) 2D cartoon and representative time series of snapshots of repetitive plane waves of NSR, a rotating spiral and its core for VT, and spatiotemporal irregularity of VF (**c**) analogous snapshots isolated slab of human left ventricular free wall (**d**) snapshots of color-coded potential, the $V = -40$ mV isosurface and filaments during VF in the anisotropic geometry of a rabbit heart

In a two-dimensional medium, the propagation velocity depends on the curvature of the wavefront, as well as rate of activity, and the wave front can be broken at regions of unidirectional conduction block. The broken wave may evolve into a high frequency circulation of excitation, in the form of an Archimedean spiral, around the core. The core acts as an organizing center that imposes its rhythm on the rest of the tissue as the tip of a

propagating wave that reenters locations far from the core once every rotation. Even in ideal, homogeneous, isotropic media, spiral waves need not rotate rigidly around a circular core, but their tip can meander in a complicated biperiodic trajectory, and in heterogeneous media will drift (Mikhailov et al. [1994](#)). Meandering, drifting spiral waves provide a conceptual model for self-limiting episodes of reentrant arrhythmias, as the the entry will terminate when the tip reaches inexcitable boundaries – the heart surfaces, or great veins and arteries. A spiral wave can be pinned onto a compact heterogeneity, such as a coronary blood vessel, if it is sufficiently large. Spiral waves in homogenous media can be stable, or, for some sets of ion channel excitation parameters, break down into spatiotemporal irregularity.

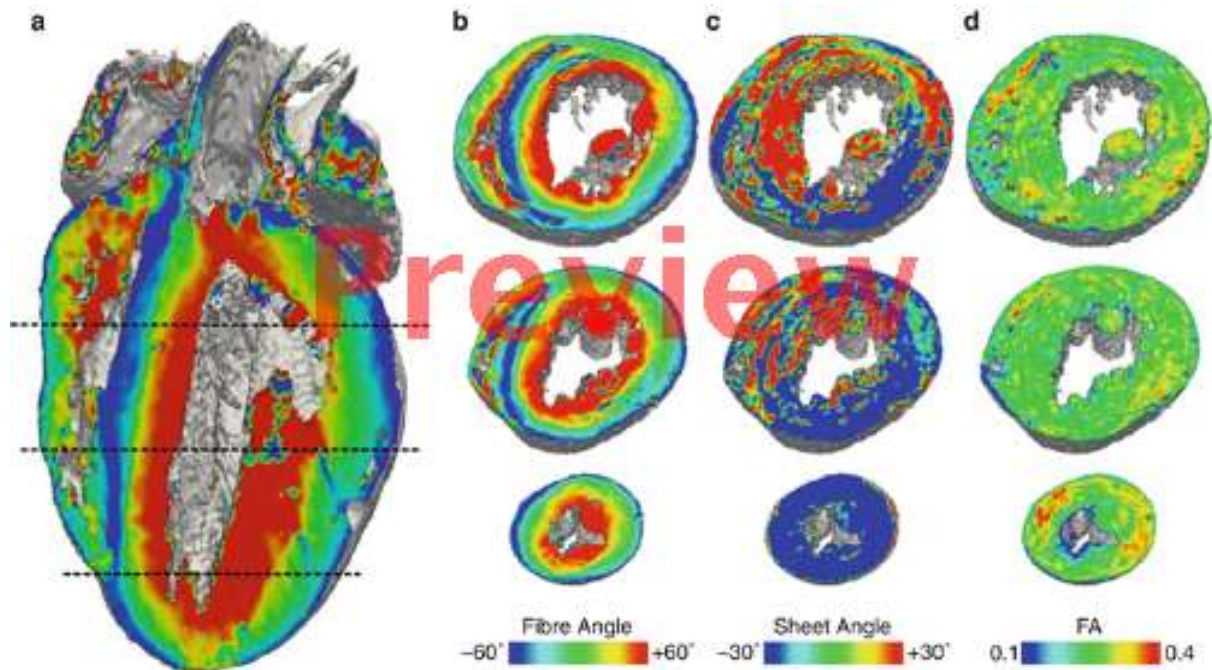
Heterogeneity enhances spiral wave instabilities.

The three-dimensional generalization of a spiral is a scroll, in which the reentry propagates around an extended, curved, meandering, and drifting filament. There are intrinsic 3D instabilities, and even in homogenous media, some sets of ion channel parameters produce stable spiral waves in 2D and unstable scroll waves in 3D.

The breakdown of spiral or scroll waves into irregularity provides mechanisms for the development of fibrillation.

Cardiac Tissue Architecture

The voltage diffusion tensor \mathbf{D} can be estimated from diffusion tensor magnetic resonance imaging (DTMRI), in which a voxel averaged diffusion tensor is calculated from the signal attenuation and the intensity of magnetic gradient applied during a diffusion weighted spin-echo experiment. The tensor is symmetric, and so the 3×3 matrix can be represented by the 3 real eigenvalues and the 3 orthogonal eigenvectors. The tensor for each voxel can be imagined as an ellipsoid whose axes are orientated along the eigenvectors, extended ellipsoids correspond to linearly extended anisotropic diffusion, flat ellipsoids to planar, orthotropic diffusion and spherical ellipsoids to isotropic diffusion. The largest (primary) eigenvector has been validated provides a measure of ventricular local average myocyte orientation within the ventricular wall of several species, and secondary and tertiary eigenvectors provide an index of any sheet orientation (Helm et al. 2005). Figure [5](#) presents fiber and sheet angles reconstructed from a DTMRI data set and illustrates the transmural change in fiber angle through the ventricles, and the more irregular sheet structure. The fractional anisotropy provides a measure of the tissue architecture, and can aid segmentation of the data set. These data sets provide the vector components of the diffusion tensor \mathbf{D} for virtual cardiac tissues. Cardiac DTMRI data sets take ~ 10 h to acquire, and so have been obtained for postmortem hearts, and a spatial resolution $\sim 100 \mu\text{m}$ can be achieved on a 9.4 T research instrument, fine enough for computing propagation.



Modeling the Heart, Fig. 5

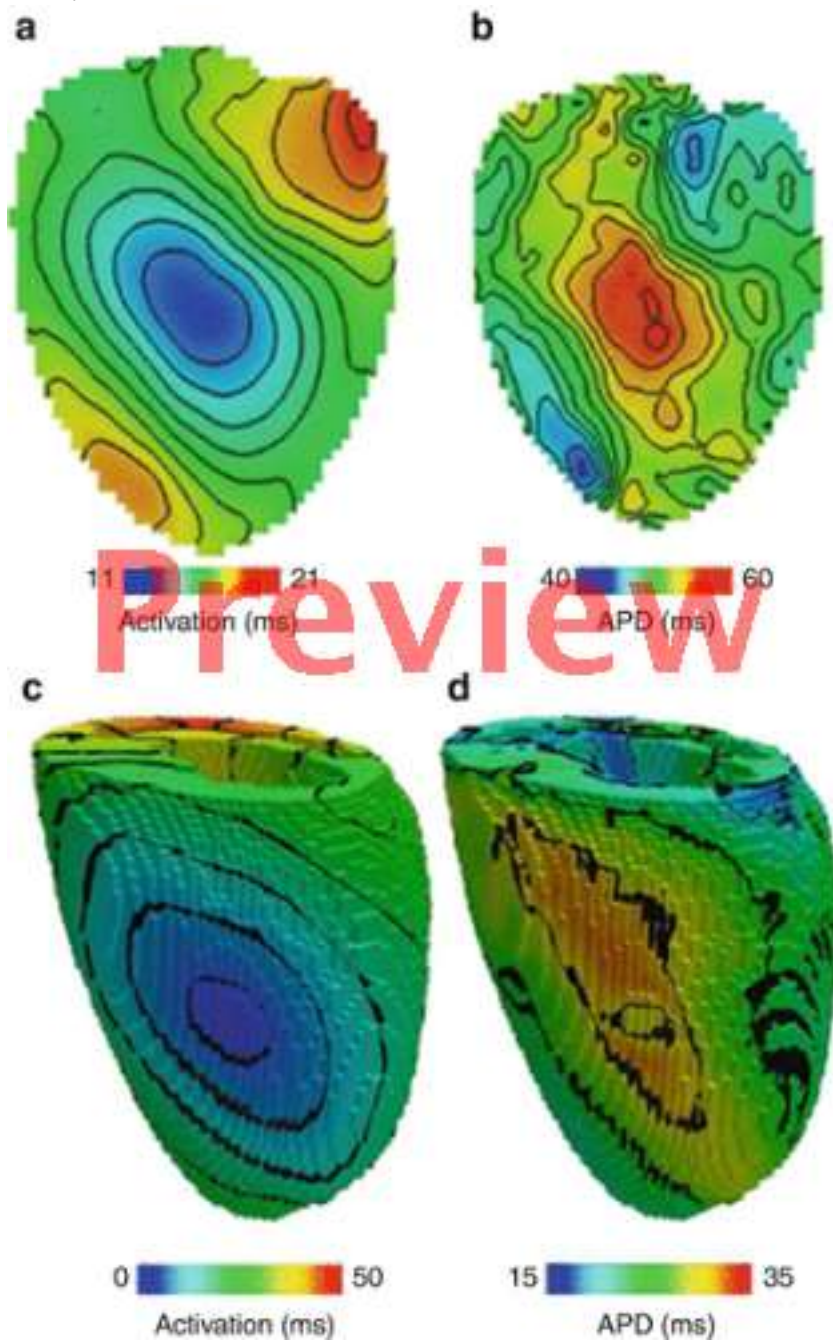
Visualization of fiber and sheet orientation, and a measure of anisotropy, for a 200 μm cubic voxel digital data set reconstruction of a rabbit heart obtained by DTMRI (**a**) long axis, (**b–d**) short axis slices. All angles are defined relative to a line through the centroids of the left ventricle

Clinical cardiac magnetic resonance imaging provides two-dimensional slices in any selected plane, or three-dimensional data sets of cardiac geometry, at a spatial resolution of 2–3 mm (Garg et al 2016), at selected times in the cardiac cycle. Patient specific ventricular geometry reconstructed from clinical imaging does not include any information about anisotropy or orthotropy: For patient specific modeling this could be introduced by rule based methods, as the smooth, transmural change of $\sim 120^\circ$ in fiber helix angle is found in all normal mammalian hearts.

Computational Systems Biology of the Heart

Myocyte excitation and action potentials are cell level properties that emerge from the interactions between membrane and intracellular ion transport processes, and the computed effects of drugs on cell behavior could be tested by experiments on cells. Synchronization and propagation are tissue level effects, and models allow the quantitative effects of different mechanisms to be dissected separately in space and time. The effects of changed channel properties (due to mutations or drugs) rate, curvature, anisotropy, and spiral wave meander patterns can be computed in isolation for homogenous virtual tissues. These quantitative spatiotemporal predictions of virtual behaviors cannot be tested experimentally, as all real cardiac tissue has an architecture and is heterogeneous. Figure 6 illustrates the visualization, using voltage sensitive dyes, of surface and subsurface electrical activity of an isolated perfused heart, where contraction has been blocked by an excitation-contraction decoupler (Walton and Bernus 2015). Such optical mapping experiments can provide a partial quantitative validation of predicted three-dimensional spatiotemporal activity during normal sinus rhythm, or solitary or periodic propagating action potentials produced by stimulation. They can only provide a semiquantitative, statistical validation of the

spatiotemporal irregularities of computed activity during fibrillation (Biktashev and Holden [2001](#)).



Modeling the Heart, Fig. 6

(a) Activation time and (b) action potential duration obtained from optical mapping of surface spatiotemporal activity in response to a brief suprathreshold stimulation in isolated, perfused rat heart, contraction blocked by and voltage imaged using Di-4-ANEPPS (c) computed activation time and (d) action potential duration

The myocardium is not just composed of myocytes there are also fibroblasts, connective tissue and intruding blood vessels, and perhaps scar tissue resulting from earlier damage. All these can contribute to non-excitable granularities, with length scales from $\sim 100 \mu\text{m}$ to cm, which can interfere with propagation, either by producing a site for wave breaking or for pinning the free ends of reentrant waves. Further functional heterogeneities emerge if

excitation is coupled to contraction in electromechanical models (Nordletten et al 2011) with mechano-electric feedback (Quinn et al 2014).

Summary

The normal sinus rhythm of the heart, reentrant arrhythmias and fibrillation can all be computed in terms of the propagation of nonlinear waves in an excitable medium, with the excitation described by membrane ion transport and intracellular sequestration and binding. Physiological and pathological patterns can be explained in terms of nonlinear wave properties – the dependence of velocity on rate by nonlinear dispersion, and breakdown from spatiotemporal patterned activity into irregularity by interactions between waves and by changes in wave stability. The anatomy of the heart – its size, shape, and organization into chambers and conducting pathways – provide the physical structure within which propagation occurs, and can be incorporated as a data set obtained from DTMRI. A biophysically and anatomically detailed computational model of mammalian heart electrophysiology can describe the electrical activity of the heart, how it is altered by drugs, or mutations in ion channels. Such quantitative predictions can be partially tested by optical recordings of activity in isolated, perfused hearts. The virtual human heart can be used to link noninvasive clinical recordings with models of the underlying cellular electrophysiology. Normal sinus rhythm, and arrhythmias, are cm length scale and 1–1,000 s time scale phenomena that emerge, at a tissue level, from the spatially heterogeneous cellular electrophysiology and tissue architecture, and the effects of changes in the ms-100 ms kinetics of ion transport processes on the initiation and persistence of arrhythmias can be computed.

Cross-References

[Analysis of Macroscopic Currents](#)

[Bioelectricity, Ionic Basis of Membrane Potentials and Propagation of Voltage Signals](#)

[Fluorescence Techniques for Studying Ion Channel Gating: VCF, FRET, and LRET](#)

[Gap Junction Proteins \(Connexins, Pannexins, and Innexins\)](#)

[Potassium Channels: Their Physiological and Molecular Diversity](#)

[Patch-Clamp Recording of Single Channel Activity: Acquisition and Analysis](#)

[Voltage-Gated Sodium and Calcium Channels](#)

References

Biktashev VN, Holden AV. Characterization of patterned irregularity in locally interacting, spatially extended systems: ventricular fibrillation. *Chaos*. 2001;11:653–64.

[PubMed](#)

Colman MA, Pinali C, Trafford AW, Zhang H, Kitmitto A, “A Computational Model of Spatio-Temporal Cardiac Intracellular Calcium Handling with Realistic Structure and Spatial Flux Distribution from Sarcoplasmic Reticulum and T-tubule Reconstructions”, Accepted PLOS

Comp Biol 28/08/2017).

<http://journals.plos.org/ploscompbiol/article?id=10.1371/journal.pcbi.1005714>

Ermentrout B, Rinzel J. Differential equations. In: De Schutter E, editor. Computational methods for neuroscientists. Cambridge, MA: MIT Press; 2009. p. 1–29.

Fink M, Niederer SA, Cherry EM, Fenton FH, Koivumaki JT, Seemann G, Thul G, Zhang H, Sachse FB, Beard D, Crampin EJ, Smith NP. Cardiac cell modelling: observations from the heart of the cardiac physiome project. *Prog Biophys Mol Biol*. 2010;104:2

[PubMed](#)

Garg P, Underwood SR, Senior R, Greenwood JP, Plein S. Noninvasive cardiac imaging in suspected acute coronary syndrome. *Nat Rev Cardiol*. 2016 May;13(5):266-75. doi: 10.1038/nrcardio.2016.18. Epub 2016 Feb 25.

PMID: 26911331

Helm P, Beg MF, Miller MI, Winslow RL. Measuring and mapping cardiac fiber and laminar architecture using diffusion tensor MR imaging. *Ann N Y Acad Sci*. 2005 Jun;1047: 296-307.

PMID: 16093505

Hille B. Ion channels in excitable membranes. Sunderland, MA: Sinauer; 2001.

Kohl P, Gourdie RG. Fibroblast-myocyte electrotonic coupling: does it occur in native cardiac tissue?

J Mol Cell Cardiol. 2014 May;70:37-46. doi: 10.1016/j.yjmcc.2013.12.024. PMID: 24412581

Leenhardt A, Denjoy I, Guicheney P. Catecholaminergic polymorphic ventricular tachycardia. *Circ Arrhythm Electrophysiol*. 2012 Oct;5(5):1044-52. doi: 10.1161/CIRCEP.111.962027.

Mikhailov AS, Davydov VA, Zykov VS. Complex dynamics of spiral waves and motions of curves. *Physica-D*. 1994;70: 1–39.

Noble D. Cardiac action and pacemaker potentials based on the Hodgkin-Huxley equations. *Nature*. 1962;188: 495–7.

Noble D, Rudy Y. Models of cardiac ventricular action potentials: iterative interaction between experiment and simulation. *Philos Trans R Soc (Lond)*. 2001;A 359:1127–42.

Nordsletten DA, Niederer SA, Nash MP, Hunter PJ, Smith NP. Coupling multi-physics models to cardiac mechanics. *Prog Biophys Mol Biol*. 2011 Jan;104(1-3):77-88. doi: 10.1016/j.pbiomolbio.2009.11.001. Epub 2009 Nov 14.

PMID: 19917304

Panfilov AV, Holden AV, editors. The computational biology of the heart. Chichester: Wiley; 1997.

Pinali C, Bennett H, Davenport JB, Trafford AW, Kitmitto A. Three-dimensional reconstruction of cardiac sarcoplasmic reticulum reveals a continuous network linking transverse-tubules: this organization is perturbed in heart failure. *Circ Res*. 2013 Nov 8;113(11):1219–30.

Priest BT, McDermott JS. Cardiac ion channels. *Channels (Austin)*. 2015;9(6):352-9. doi: 10.1080/19336950.2015.1076597. Epub 2015 Aug 20. Review. PMID: 2655655

Qu Z, Hu G, Garfinkel A, Weiss JN. Nonlinear and Stochastic Dynamics in the Heart. *Phys Rep*. 2014 Oct 10; 543(2): 61–162. doi: 10.1016/j.physrep.2014.05.002
PMCID: PMC4175480

Quinn TA, Kohl P, Ravens U. Cardiac mechano-electric coupling research: fifty years of progress and scientific innovation. *Prog Biophys Mol Biol*. 2014 Aug;115(2-3):71-5. doi: 10.1016/j.pbiomolbio.2014.06.007
PMID: 24978820

Roberts BN, Yang PC, Behrens SB, Moreno JD, Clancy CE. Computational approaches to understand cardiac electrophysiology and arrhythmias. *Am J Physiol Heart Circ Physiol*. 2012 Oct 1;303(7):H766-83. doi: 10.1152/ajpheart.01081.2011. PMID: 22886409

Ten Tusscher KHW, Panfilov AV. Alternans and spiral breakup in a human ventricular tissue model. *Am J Physiol Heart Circ Physiol*. 2006;291:H1088–100.
PubMed

Trayanova NA. Mathematical approaches to understanding and imaging atrial fibrillation: significance for mechanisms and management. *Circ Res*. 2014 Apr 25;114(9):1516-31. doi: 10.1161/CIRCRESAHA.114.302240. PMID: 24763468

Walton RD, Bernus O. Towards Depth-Resolved Optical Imaging of Cardiac Electrical Activity. *Adv Exp Med Biol*. 2015;859:405-23. doi: 10.1007/978-3-319-17641-3_16.
PMID: 26238062

Winfree AT. *The geometry of biological time*. 2nd ed. New York: Springer; 2001.